Automatic Ship Detection in Satellite Multispectral Imagery

Abstract

In recent years, very little attention in the literature has been given to the task of automatically detecting shipping vessels in optical satellite imagery. A method for achieving this goal is described for both SPOT Multispectral and Landsat Thematic Mapper data. Essentially a task in pattern recognition, the method utilizes masking, filtering, and shape analysis techniques. Results showing a high degree of accuracy have been obtained with test data.

Introduction

Situated in the south pacific ocean, New Zealand relies heavily on its international shipping activities both for trade and with respect to its fishing industry. Because the territorial waters of New Zealand are so extensive, when compared to the land mass, monitoring shipping movements is difficult and costly. This present study has been motivated by an interest in assessing the multispectral data now available, for its usefulness in tracking the movement of shipping in the waters of the large Exclusive Economic Zone surrounding New Zealand. In 1978 McDonnell and Lewis (1978) showed that detection of large ships was theoretically possible with Landsat multispectral data. With a ground resolution of only 79 m, these data have now been superseded by both SPOT multispectral and Landsat TM data, at 20-m and 30-m resolution, respectively.

Although operationally monitoring shipping movements with optical data alone is not a realistic possibility due to the somewhat severe constraints of cloud cover and scene illumination, the improved resolution has prompted renewed interest in the area, with the objective of assessing what new information is revealed and how adequately the process can be automated.

Previous Work

Past work in the area of remote sensing of ships and ship wakes is sparse and tends to concentrate more on characterizing a visually identified wake, than on techniques for automatic detection. The 1986 Bakerian Lecture of the Royal Society of London (Munk *et al.*, 1987), entitled "Ships from Space," gave a comprehensive treatment of wake geometry, comparing the classic Kelvin wake as seen in optical images with the long "V"-like trail which results from Bragg scattering in Synthetic Aperture Radar (SAR) images. Unexpected "V"-like wakes in optical images returned from a 1985 space shuttle mission were explained in terms of sun glitter from the titled facets of a Kelvin wake. Lyden (1988) also analyzed wake structure and identified three general categories into which wake phenomena could be classified: surface waves generated by the ship, turbulent or vortex wakes, and internal waves. The visibility of the various wake features was compared under various conditions such as wind speed and SAR look direction.

Peltzer (1987), in his paper entitled "A Remote Sensing Study of a Surface Ship wake," presented results of an investigation into the effect of a monomolecular film on the surface of the turbulent wake. The wake was imaged using a thermal infrared scanner, an X-band coherent microwave radar, and a 35-mm strip camera, all aircraft mounted. It was found that the film attenuated the wake response in the X-band images and led to greater persistence of the wake in the thermal image. This was because the film reduced the surface roughness and prevented wind driven mixing of the cool wake with the surrounding warmer water.

Work done specifically in the area of ship detection has commonly utilized data from one of two disparate sources: SAR and Forward Looking Infrared (FLIR). In their assessment of ocean surface phenomena in Seasat SAR imagery, Vesecky and Stewart (1982) identified a number of factors which influenced visual identification. These included the sea state, winds, currents and ship size, speed, and orientation with respect to the radar. Chang (1985) also used Seasat SAR data to demonstrate a trace confirmation algorithm for ship detection. Bright spots were first identified in the image, which were possibly moving ships; then a sector sweeping approach was used to detect the ship's wake. If there existed a sector around a bright spot, for which the response was significantly higher than neighboring sectors, a wake was considered to be detected and the bright spot was confirmed as a ship.

By far the greatest effort in the area of ship detection has been made in the military arena, within the scope of automatic target recognition (ATR) systems. These systems invariably utilize FLIR imagery, often provided by aircraft mounted sensors (Bhanu,1986; Lahart,1984). They not only automatically detect targets, but also classify them, prioritize individual targets in the field of view, track them in real time, and select aimpoints. Although the resolution and information content in FLIR imagery bears very little resemblance to that of satellite based optical systems, there is some commonality in the techniques that can be utilized. Many ATR systems use classical pattern recognition methodology combined with an artificial intelligence knowledge-base approach (Bhanu,1986). Contextual information such as map and sensor data, intelligence information, and seasonal variation are used to improve accuracy and sensitivity.

The algorithm for automatic ship detection which will be outlined in subsequent sections also makes use of problem knowledge. The search domain is first restricted to the

Deborah W. Burgess*
Information Technology Group, DSIR Physical Sciences, P. O. Box 31-311, Lower Hutt, New Zealand

*Presently with Landcare Research New Zealand Ltd, P. O. Box 38-491, Wellington Mail Centre, New Zealand.

Photogrammetric Engineering & Remote Sensing, Vol. 59, No. 2, February 1993, pp. 229–237.

0099-1112/93/5902–229$03.00/0

areas of water in the scene. A series of filters are used to remove extraneous information, while preserving the integrity of any ship data which may be present. All remaining objects are considered to be potential ships. Size, shape, and intensity measures are then used to refine the set, culminating in the production of a ship location report detailing the location, size, and heading of the ships found.

The Original Data

The three bands of SPOT XS show distinct contrasts in terms of the responses to various sea features. Band 1 data highlights sediments and currents and shows ship wakes clearly. This can be seen in Figure 1a, which shows band 1 of a SPOT test image of Wellington Harbour, New Zealand. Band 3, however, often has negligible response to any sea feature. Closer inspection of the lower end of the data in this band reveals that ship wake information *is* present and the signal-to-noise ratio is better than that of band 1, due to the "flat" background which the ship wake is set against. This is illustrated in Figure 1b, which shows band 3 of the SPOT test image with the data stretched between counts of 0 and 15. For SPOT scenes, therefore, it was decided to use a combination of band 1 and band 3, utilizing the high contrast obtained in band 3 and the extra wake information available in band 1.

Landsat TM, with seven spectral bands, offers a greater number of options. Because band 4 of the TM data is the near infrared band, it is not surprising that the response of this band to ship wakes is similar to that of SPOT band 3 which is also near infrared. Landsat band 3 also showed good response to ship wakes; therefore, these two bands have been used when processing Landsat TM scenes. Figure 2 shows these bands for a TM test image of an area just outside Auckland Harbour, New Zealand.

In this paper the term *input image 1* is used to refer to SPOT band 1 or Landsat band 3 and *input image 2* for SPOT band 3 or Landsat band 4.

Preprocessing

There are four preprocessing stages performed, which are as follows:

- Masking out the land in each input image,
- High pass filtering each image,
- Selectively combining the images, and
- Trim filtering the combined image.

The first three stages are independent of the data source; however, the fourth stage is only performed on images originating from the SPOT satellite to overcome sensor calibration anomalies.

In order to make a land mask, it was first necessary to find a point-wise operation which gave adequate discrimination between land and sea pixels. A heuristic approach has been taken based on observations of the relationship between the data values in the two input images for each class type.

If $I_i(x,y)$ represent pixel y on line x in input image i and $D(x,y)$ is the binary discrimination image, which is zero (land) when the test returns false and one (sea) when the test returns true, then the necessary operation for SPOT data is

$$D(x,y) = \left(\frac{I_1(x,y)}{I_2(x,y)} > 3.5 \right)$$

and for Landsat data is

$$D(x,y) = (I_2(x,y) < I_1(x,y))$$

This discrimination image, which is illustrated in Figure 3a for the SPOT test scene, provides a starting point for making a land mask. Its accuracy is generally good, apart from some speckling in both the land and sea regions and the significant fact that ships are often classified as land.

A low pass filter is used to remove ships from the mask and improve the consistency of the image. An efficient implementation of a box filtering approach is used for the purpose (McDonnell, 1980) with a 41 by 41 square box. This

(a) Band 1

(b) Band 3

Fig. 1. SPOT test image (©CNES 1989).

size box has been chosen because it is large with respect to the anticipated size of ships and their wake and, as such, has the effect of removing the high frequency response to the ships, blurring the coastline, and removing fine speckle. It should be noted that at this point ships, small islands, and isolated clouds are all treated alike.

A threshold is then used to regain a binary land mask with the land area extended into the sea. The land area is shrunk back to the true coastline using a 3 by 3 window rank filter with rank 9 (Hodgson, *et al.*,), also known as a Maximum filter. Because of the rank filter's ability to propagate edges, each application of the Maximum filter strips the border pixels from the land area and thus shrinks the land mask. Figure 3b shows the result of five applications of the filter, which has trimmed the land mask boundary to within a small margin of the coastline.

The resultant binary image is used as the land mask and is applied to each of the input images so that the land pixels are set to the mean sea count (Figures 3c and 3d). Using this approach, rather than just setting the land area to a count of zero, ensures that there is no sharp gradient between the masked area and the sea. This improves the result of the high pass filter, which is applied next.

The high pass filter, applied to the two masked images, smooths out the slowly varying background caused by current flows and sediment (Figures 3e and 3f). Again, a 41 by 41 filter window is used because this is relatively large compared to the expected target size. This has the effect of setting the background to zero and small sea features to counts relative to the surrounding sea. This filter works well, although sparse areas of low valued noise remain in the resultant images. Because of the different response characteristics of the original bands used, there seems to be little correlation between the noise remaining in each image at this stage.

The two filtered images need to be combined in such a way that all the shape information is preserved while the noise is not reinforced. This makes a simple addition inappropriate; instead, the approach taken is to use image 1 where it is non-zero and accept image 2 elsewhere. This means that, in the combined image, ships and their wakes get shape information from both input images. Figure 4 shows the different shape information provided by each of the filtered images for the large ship in the SPOT scene which is labeled as 3 in Figure 8a. The typical situation is illustrated where image 1 contributes information about the shape of the turbulent far wake and image 2 contains more non-zero pixels on the leading edge.

Often in SPOT data there exists a low valued vertical striping in the third band with a count one above the background. This is due to the uneven calibration of the original CCD sensors used to collect the data. It is not normally noticeable in the level 1A imagery and is not apparent in the images of Figure 3; however, at this stage in the preprocessing it usually becomes quite evident. Therefore, a 3 by 3 trim filter is used, only in the case of SPOT data, to remove this effect. The center pixel is set to zero if six or more of the pixels in the window are zero. This has the effect of removing single pixel wide lines and "chopping up" others. There is negligible effect on the target ships and their wakes.

Analysis

Figure 5 shows the images after preprocessing is complete. Each image is predominantly zero apart from small sea features such as rocks, islands, small cloud, scattered noise, and ships. As a starting point, each distinct object, defined as having no 8-connected non-zero neighbors, is considered to be a possible ship. This connectivity convention is chosen because the tail of a ship wake often consists of only diagonally connected pixels. Recognizing these pixels as part of the wake is critical to discriminating the ship wake shape from other less elongated objects.

A one-pass scan conversion algorithm (Bell, 1973) is used to build a contour sequence of each object boundary which is used during analysis as a representation of the ob-

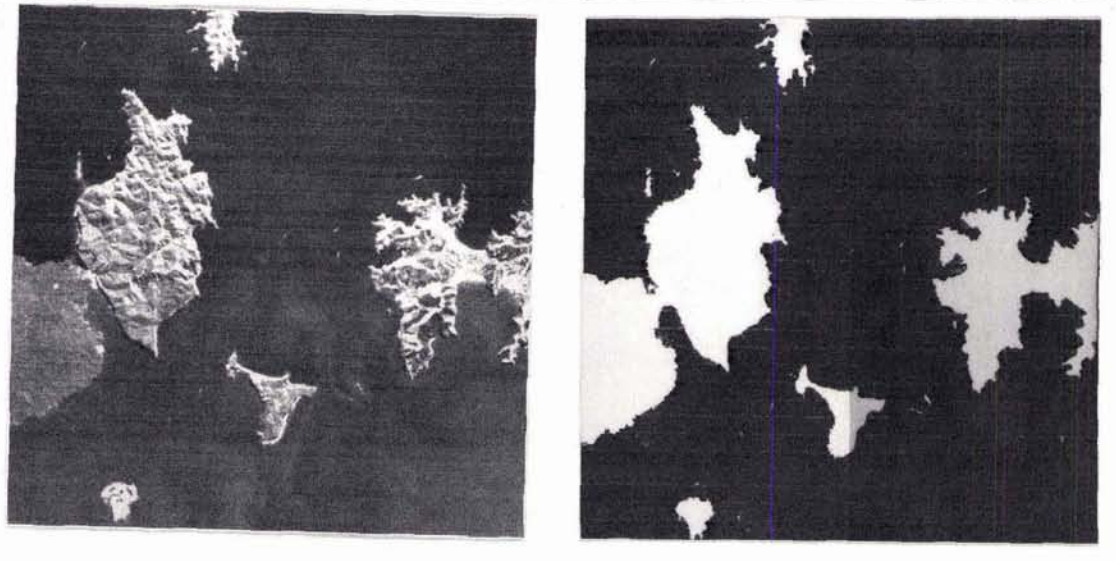

(a) Band 3 (b) Band 4

Fig. 2. Landsat TM test image (©EOSAT 1989).

(a) discrimination image

(b) land mask

(c) Image 1 masked

(d) Image 2 masked

(e) Image 1 masked and high pass filtered

(f) Image 2 masked and high pass filtered

Fig. 3. Steps in preprocessing the SPOT test scene (©CNES 1989).

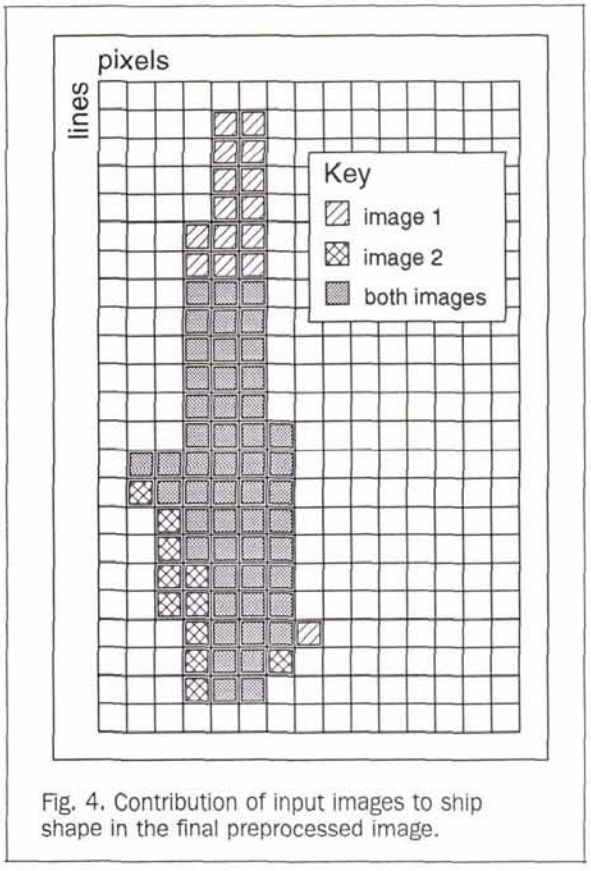

Fig. 4. Contribution of input images to ship shape in the final preprocessed image.

ject shape. The class of possible ships is gradually refined by performing a series of tests to see whether individual objects meet certain ship criteria.

Refinement by Area

Naturally, only objects of a realistic size should be considered as potential ships. Areas are calculated using a discrete application of Green's theorem (Riddle, 1984). The object area is defined as the area in square pixels inside the line joining the center of the border pixels. Because it is possible for ships to be smaller than one pixel for either of the sensors under discussion, the lower size limit was set according to the smallest object that could be positively identified in the image. An area of three square pixels was chosen as the lowest valid area. The upper size limit represents the largest area that a ship and its wake could be expected to cover. The purpose of the upper limit is generally to rule out "obviously" oversized objects such as clouds and islands. It is a coarse method of selection for which threshold value is not critical. A value of 150 square pixels has been chosen to allow a "margin of safety," i.e., very large objects are ruled out early in the analysis but those that are questionable are retained to be analyzed and possibly rejected by one of the more computationally intensive refinement procedures. Because the upper limit of 150 is not critical, the value is used with both SPOT and TM data.

Refinement by Shape Analysis

Once unrealistically sized objects have been ruled out, a study is made of the shape of each remaining object. A measure of the elongation of the object is needed to identify those objects which conform to the typical profile of a large ship or ship and its wake. Clearly, it is important to use a shape measure which is position and orientation independent. This is achieved using a form of moment analysis (Hu, 1962; Smith, 1971). The generalized formula for the simple moment M_{ij} is as follows:

$$M_{ij} = \int\int_R x^i y^j f(x,y)\, dx\, dy \qquad (1)$$

where R is a finite region over which $f(x,y)$ exists and i and j are integers.

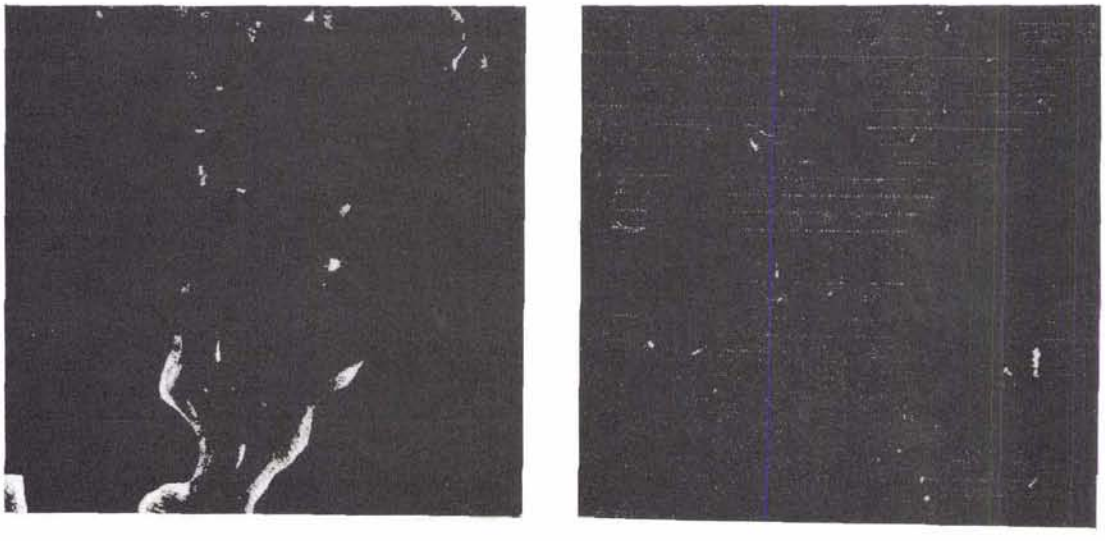

(a) SPOT (b) Landsat TM

Fig. 5. Final preprocessed test images with the input images masked, filtered, and combined.

By the Uniqueness Theorem (Hu, 1962), the moment sequence $\{M_{ij}\}$ is uniquely determined by $f(x,y)$ and $f(x,y)$ is uniquely determined by $\{M_{ij}\}$; therefore, it can be said that $\{M_{ij}\}$ characterizes the shape of $f(x,y)$. In practice, most of the coarse shape information is contained in the first few low-order moments with higher order moments adding the higher frequency shape components. A combination of low-order moments has therefore been used as a measure of object elongation.

Because only the shape is being considered, it is possible to simplify Equation 1 by setting $f(x,y) = 1$ inside the object and $f(x,y) = 0$ outside. This gives

$$M_{ij} = \int\int_B x^i y^j \, dx \, dy \tag{2}$$

where B is the region occupied by the object being considered.

Moments generated from Equation 2 are not position or orientation independent. They depend on the location of the object with respect to the origin and its orientation with respect to the x and y axes. To achieve position independence, moments are calculated using the object centroid as the origin. The coordinates of the centroid $(\bar{x},\bar{y})$ are defined as

$$\bar{x} = \frac{M_{10}}{M_{00}}, \quad \bar{y} = \frac{M_{01}}{M_{00}} \tag{3}$$

where $M_{00} = \int\int_B dx,dy$ is simply the area of the object.

The first moments, required to calculate the centroid, are found by applying a discrete method of evaluation (Freeman, 1961) which uses the object border in chain code form. Central moments, found by taking the centroid as the origin, can then be calculated as follows:

$$m_{ij} = \int\int_B (x - \bar{x})^i (y - \bar{y})^j dx \, dy \tag{4}$$

Central moments are translation invariant but not rotation invariant. It can be shown that, if the (x,y) axis is rotated through an angle θ, the rotated moment is given by

$$\mu_{ij} = \int\int_B ((x - \bar{x}) \cos\theta + (y - \bar{y}) \sin\theta)^i + (-(x - \bar{x}) \sin\theta + (y - \bar{y}) \cos\theta)^j \, dx \, dy \tag{5}$$

Because m_{10} and m_{01} are zero by definition, so too are μ_{10} and μ_{01} for all values of θ; therefore, we take the second moments μ_{20} and μ_{02} which can be written as

$$\mu_{20} = \int\int_B ((x - \bar{x}) \cos\theta + (y - \bar{y}) \sin\theta)^2 dx \, dy \tag{6}$$

$$\mu_{02} = \int\int_B (-(x - \bar{x}) \sin\theta + (y - \bar{y}) \cos\theta)^2 dx \, dy \tag{7}$$

These may be reduced to terms of m_{ij} as follows:

$$\mu_{20} = \frac{1}{2}(m_{20} + m_{02}) + \frac{1}{2}(m_{20} - m_{02}) \cos 2\theta - m_{11} \sin 2\theta \tag{8}$$

$$\mu_{02} = \frac{1}{2}(m_{20} + m_{02}) + \frac{1}{2}(m_{02} - m_{20}) \cos 2\theta - m_{11} \sin 2\theta \tag{9}$$

The values of each of these moments change as θ is varied. If μ_{02} is minimized, then the resulting angle θ should define the axis from which the edges of the shape deviate least, i.e., in the case of a ship and wake, the axis should lie along the direction of travel. In order to find the minimum μ_{02}, $d\mu_{02}/d\theta$ is found and set equal to zero. This gives

$$\tan 2\theta_p = \frac{2m_{11}}{(m_{20} - m_{02})} \tag{10}$$

Clearly, this may yield either the minimum or the maximum, so a check is performed. Defining μ'_{ij} to be μ_{ij} when $\theta = \theta p$, θp is set to $\theta p + \pi/2$ if $\mu'_{02} > \mu'_{20}$. The axis defined by θp is called the *principal axis* (see Figure 6). The second-order moments μ'_{02} and μ'_{20} for any given object are size, position, and orientation independent.

A good measure of elongation is the ratio $\mu'_{02} : \mu'_{20}$. A threshold level of 0.2 has been selected because this gives correct discrimination on test data. For many larger ships, the calculated value will be as low as 0.01. It has been recognized that this measure is less appropriate for smaller vessels, where the pixels occupied by the craft often depend more on its location with respect to pixel boundaries than on

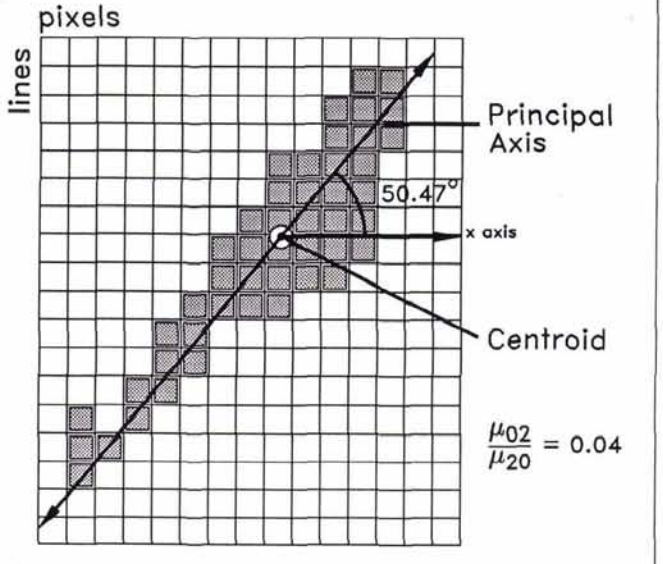

Fig. 6. Principal axis of ship profile.

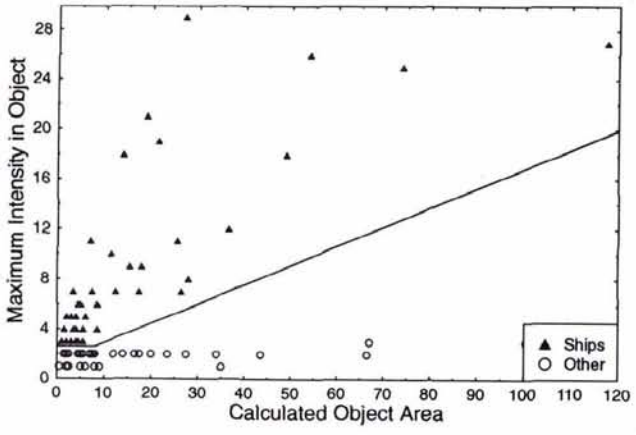

Fig. 7. Relationship of object maximum intensity to object area.

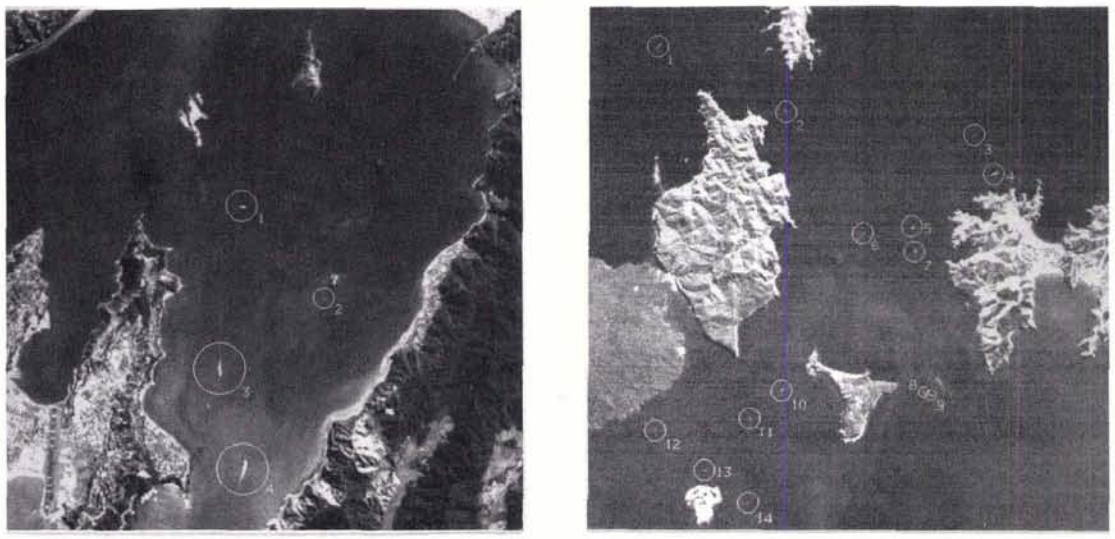

(a) SPOT (©CNES 1989) (b) Landsat TM (EOSAT 1989)

Fig. 8. Ships automatically located in test scenes.

its actual shape. For that reason, the ratio threshold of 0.2 is relaxed for objects of small area. Specifically, the threshold is varied linearly between 0.2 and 0.4 for areas in the range 8 to 3 pixels.

Refinement by Maximum Intensity

Those objects that pass the shape criteria are tested to establish whether they are just conveniently shaped noise, or something more significant. Each object in the class of possible ships is scanned in the preprocessed image to determine its highest pixel count. The brightness of a ship and wake system is linked to its size; therefore, an area dependent threshold is used to discriminate between ships and noise. Figure 7 shows the relationship between object size and maximum intensity in the preprocessed image for a range of ships and other objects. It can be seen from the graph that the solid line which indicates the threshold used levels off for small objects. This is because a lower limit has been set on the maximum intensity, requiring that it be at least three counts above the background, which corresponds to a value of 3 in the preprocessed image. A maximum of only 1 or 2 counts above the background must be considered as resulting from noise even though under certain favorable conditions positive visual identification can be made for very small boats with these maximums. The implication here is that very small craft will not be detected by the system. This is true; however, the level at which the system fails is close to the level where there is insufficient information for visual identification.

Refinement by Spectral Signature

Having reduced the class of possible ships to a set of objects of the appropriate size and shape to be ships which contain at least one bright pixel, the task is almost complete. Objects which have been incorrectly retained at this stage are often small islands. In the case of Landsat TM data, this problem can be overcome using standard classification techniques. A Bayes classification (Colwell, 1983) is done on bands 1, 2, and 3 of the original Landsat data using statistics calculated from the three bands, with the original land mask as a training field. Objects in the class of potential ships are scanned in the classification image. If any of their pixels are classified as land, they are rejected.

Unfortunately, the distinction between the spectral signatures of ships and land is not so clear in SPOT XS data.

TABLE 1. SHIPS DETECTED IN SPOT TEST IMAGE

Ship ID	Location (NZ Map Grid)	Heading (degrees)	Length of ship + wake (metres)
1	5990073,2664943	−13.1	165
2	5988255,2666541	200.1	63
3	5986908,2664512	−89.6	400
4	5984952,2664964	76.0	475

TABLE 2. SHIPS DETECTED IN LANDSAT TM TEST IMAGE

Ship ID	Location (line,pixel)	Heading (degrees)	Length of ship + wake (metres)
1	42,68	46.9	339
2	105,193	109.5	134
3	127,377	—	108
4	165,396	25.7	362
5	216,316	227.8	127
6	223,268	40.2	108
7	241,319	84.2	180
8	377,329	—	124
9	380,336	−30.1	201
10	376,190	69.7	218
11	403,159	113.5	108
12	415,67	31.7	134
13	453,115	26.0	201
14	485,158	241.8	175

When Landsat bands 1, 2, and 3 are mapped to blue, green, and red, respectively, ship wakes appear white. However, under the same mapping, SPOT scenes show cyan wakes in a range of shades common in urban areas and present in rural terrain.

Final Calculations

Many of the previous measurements rely on the assumption that the entire area of the object is represented in the image. This cannot be guaranteed if the object is at the edge of the image, or if it has been partially occluded by the land mask during preprocessing. Under these circumstances, the size and shape measurements may not be a true indication of the characteristics of the whole object; therefore, objects that fall into this category are rejected.

Further information is extracted from those objects remaining, all of which are deemed to be identified ships. First, a measure of the length of the ship-and-wake system along the principle axis is made. Efforts to distinguish the ship from its wake have been unsuccessful, so this length is dependent both on the ship size and its speed.

The principle axis calculated previously gives an indication of the orientation of the vessel, but there are still two possible choices for the heading, i.e., θp or $\theta p + \pi$. A robust peak detection method (O'Gorman, 1984) is used to find the intensity peak for each ship. The heading is then chosen to coincide with the side of the centroid containing the peak. Occasionally, the distance between the centroid and the intensity peak is considered too small to make a decision.

Discussion of Results

Examples of the type of output obtained from the detection algorithm can be seen in Tables 1 and 2. A "-" in the Heading column indicates that the program was unable to clearly identify the heading. The type of location that is reported depends on whether the original data have been rectified or not. In the case of the SPOT data, the scene has been rectified to the New Zealand Metric Map Grid (Reilly, 1977); therefore, the locations are given in these coordinates. The TM data, conversely, have not been rectified; therefore, image coordinates are used.The locations of the identified craft have been circled in Figure 8. Each craft has been visually confirmed in the image and no clearly identifiable ships appear to have been missed. No ground truth data are available for the TM scene; however, shipping records allow identification to be made of the three larger vessels in the SPOT scene. Using the numbering scheme of Figure 8, they are

1 Eastbourne Ferry, length = 18.5m, speed = 20 knots
2 Unknown
3 South bound InterIslander Ferry, the "Aratika," length = 127m, speed = 17 knots
4 North bound InterIslander Ferry, the "Arahunga," length = 127.4m, speed = 17 knots

Vessel 2 identified in the SPOT scene is probably only a small pleasure craft, as are the majority of those present in the TM scene. In these cases nautical charts were checked to ensure that there were no rocks, lights, or other irregularities which might have been detected. Examination of charts also ensured that the position in question was a viable place for a ship to be located.

An elongated shape, which has not been detected as a ship, can be seen in the TM image, southeast of the image center, in the proximity of ships 8 and 9. In a color image, this can be easily identified as an island. This is a classic example of the type of object which makes spectral analysis necessary. Because spectral analysis has only proved feasible with TM data, an island such as this, in a SPOT image, will cause a false alarm. As mentioned previously, there is also a lower limit on the size of craft which can be automatically detected. At least seven pixels must have counts above the background to give a border linked area of three square pixels, and at least one of these must have a value at least 3 counts above the background before the object is considered as a potential ship. The human eye is often able to detect a ship based on much less information.

Conclusions

The feasibility of automatically detecting ships and their wakes in SPOT and Landsat TM imagery has been demonstrated with a good level of accuracy. SPOT bands 1 and 3 and Landsat bands 3 and 4 have proved most useful for the purpose. A process of elimination is used which discards objects which fail the ship criteria of size, shape, intensity, and color. Relatively small craft can often be identified if traveling at speed because a long wake is generated.

Although the detection of ships from optical imagery is hampered by cloud cover and low illumination, the accuracy obtainable under favorable conditions makes the techniques extremely worthwhile. It is felt that ideally an automatic shipping surveillance system should combine data from a number of different sensors. In particular, Synthetic Aperture Radar imagery, which is unaffected by cloud cover or illumination, would be complementary.

Acknowledgments

I would like to thank Dr. David Pairman and Dr. Steven McNeill from the Information Technology Group of DSIR Physical Sciences for their support, advice, and encouragement throughout the course of this work.

References

Bell, D. A., 1973. *The Extraction of Continuous Boundaries and Contours from a Raster Scan*, NPL Report COM66, National Physics Laboratory, Division of Computer Science, United Kingdom.

Bhanu, B., 1986. Automatic Target Recognition : State of the Art Survey, *IEEE Trans. on Aerospace and Electronic Systems*, Vol. AES-22, No. 4, pp. 364–379.

Chang, S. K., Bingwei Luo, C. C. Yang, and M. C. K. Yang, 1985. Trace Confirmation with Given Object Position, *Int. J. of Computer and Information Sciences*, Vol. 14, No. 6, pp. 439–453.

Colwell, R. N., 1983. *Manual of Remote Sensing*, American Society of Photogrammetry, pp. 795–800.

Freeman, H., 1961. Techniques for the Digital Analysis of Chain-Coded Arbitrary Plane Curves, *Procs. of the National Electronics Conf.*, Chicago, Vol. 17, pp. 421–432.

Hodgson, R. M., D. G. Naylor, A. L. M. Ng, and S. J. McNeill, 1985. Properties, Implementations and Applications of Rank Filters, *Image and Vision Computing*, Vol. 3, No. 1, pp. 3–14.

Hu, M. K., 1962. Visual Pattern Recognition by Moment Invariants, *IRE Trans. on Information Theory*, IT 8, No. 2, pp.179–187.

Lahart, M. J., 1984. Object Identification from Images of Variable Scale, *Optical Engineering*, Vol. 23, No. 6, pp. 710–715.

Lyden, J. D., R. R. Hammond, D. R. Lyzenga, and R. A. Shuchman, 1988. Synthetic Aperture Radar Imaging of Surface Ship Wakes, *J. of Geophysical Research*, Vol. 93, No. c10, pp. 12,293–12,303.

McDonnell, M. J., 1980. *Box Filtering Techniques*, Computer Science Technical Report, University of Maryland.

McDonnell, M. J., and A. J. Lewis, 1978. Ship Detection from Landsat Imagery, *Photogrammetric Engineering & Remote Sensing*, Vol. 44, No. 3, pp. 297–301.

McNeill, S. J. E., 1987. *A System for Development of Machine Vision Systems*, PhD Thesis, University of Canterbury, pp. 134–135.

Munk, W. H., P. Scully-Power, and F. Zachariasen, 1987. Ships from Space, *Proc. Royal Soc. London*, Vol. A 412, pp. 231–254.

O'Gorman, L., and A. C. Sanderson, 1984. The Converging Squares Algorithm: An Efficient Method for Locating Peaks in Multidimensions, *IEEE Trans. on Pattern Analysis and Machine Intelligence*, Vol. PAMI-6, No. 3, pp. 280–288.

Peltzer, R. D., W. D. Garrett, and P. M. Smith, 1987. A Remote Sensing Study of a Surface Ship Wake, *Int. J. Remote Sensing*, Vol. 8, No. 5, pp. 689–704.

Reilly, W. I., 1977. A National Coordinate System, *New Zealand Surveyor*, Vol. 28, No. 6, pp.738–740.

Riddle, D. F., 1984. *Calculus and Analytical Geometry*, Wadsworth Inc., pp. 1090–1096.

Smith, F. W., and M. H. Wright, 1971. Automatic Ship Photo Interpretation by the Method of Moments, *IEEE Trans. on Computers*.

Vesecky, J. R., and R. H. Stewart, 1982. The Observations of Ocean Surface Phenomena Using Imagery from the Seasat Synthetic Aperture Radar: An Assessment, *J. of Geophysical Research*, Vol. 87, No. c5, pp. 3397–3430.

(Received 2 March 1992; Accepted 21 July 1992; Revised 10 August 1992)

FORTHCOMING ARTICLES

Richard Aspinall and *Neil Veitch*, Habitat Mapping from Satellite Imagery and Wildlife Survey Data Using a Bayesian Modeling Procedure in a GIS.

Russell G. Congalton, Kass Green, and *John Teply*, Mapping Old Growth Forests on National Forest and Park Lands in the Pacific Northwest from Remotely Sensed Data.

Russell G. Congalton and *Kass Green*, A Practical Look at the Sources of Confusion in Error Matrix Generation.

Jean-Pierre Djamdji, Albert Bijaoui, and *Roger Maniere*, Geometrical Registration of Images: The Multiresolution Approach.

John R. Dymond, An Improved Skidmore/Turner Classifier.

Douglas G. Goodin, Luoheng Han, Rolland N. Fraser, Donald C. Rundquist, and *Wesley A. Stebbins*, Analysis of Suspended Solids in Water Using Remotely Sensed High Resolution Derivative Spectra.

Edwin J. Green, William E. Strawderman, and *Teuvo M. Airola*, Assessing Classification Probabilities for Thematic Maps.

John R. Jensen, Sunil Narumalani, Oliver Weatherbee, and *Halkard E. Mackey, Jr.*, Measurement of Seasonal and Yearly Cattail and Waterlily Changes Using Multidate SPOT Panchromatic Data.

Chris L. Lauver and *Jerry L. Whistler*, A Hierarchical Classification of Landsat TM Imagery to Identify Natural Grassland Areas and Rare Species Habitat.

Oğuz Mftolu, A Data Reduction Approach Using the Collinearity Model from Non-Metric Photography.

M. Nazim, SOM Equations with Modifications to Estimate Longitude from Ascending Node, and Constants for the Clarke and Everest Spheroids.

Scott A. Samson, Two Indices to Characterize Temporal Patterns in the Spectral Response of Vegetation.

I. Tannous and *B. Pikeroen*, Parametric Modeling of Spaceborne SAR Image Geometry Application: SEASAT/SPOT Image Registration.

Gregory S. Tudor and *Larry J. Subarbaker*, GIS Orthographic Digitizing of Aerial Photographs by Terrain Modeling.

Yong-Jian Zheng, Digital Photogrammetric Inversion: Theory and Application to Surface Reconstruction.

Special March 1993 Issue
Remote Sensing for Marine and Coastal Environments

P. Bauer, S. Gaito, J. M. McGlade, and *D. Winter*, Estimation of Net Photosynthetically Available Radiation Over Oceans from Satellite Data: Application to a Dynamical Model of a Plankton Bloom in the Atlantic Ocean.

P. N. Bierwirth, T. J. Lee, and *R. V. Burne*, Shallow Sea-Floor Reflectance and Water Depth Derived by Unmixing Multispectral Imagery.

K. L. Carder, R. G. Steward, R. F. Chen, S. Hawes, and *S. Lee*, AVIRIS Calibration and Application in Coastal Oceanic Environments: Tracers of Soluble and Particulate Constituents of the Tampa Bay Coastal Plume.

L. Estep and *R. Arnone*, Correlation of CZCS Surface Ks with Ks Derived from Secchi Disk.

Johnny A. Johannessen, Lars P. Red, Ola M. Johannessen, Geir Evensen, Bruce Hackett, Lasse H. Pettersson, Peter M.Haugan, Stein Sandven, and *Robert Shuchman*, Monitoring and Modeling of the Marine Coastal Environment.

Gerald M. Korenowski, Glenn S. Frysinger, and *William E. Asher*, Noninvasive Probing of the Ocean Surface Using Laser-Based Nonlinear Optical Methods.

George A. Leshkevich, David J. Schwab, and *Glenn C. Muhr*, Satellite Environmental Monitoring of the Great Lakes: A Review of NOAA's Great Lakes CoastWatch Program.

Joseph J. Luczkovich, Thomas W. Wagner, Jeffrey L. Michalek, and *Richard W. Stoffle*, Discrimination of Coral Reefs, Seagrass Meadows, and Sand Bottom Types from Space: A Dominican Republic Case Study.

Jeffrey L. Michalek, Thomas W. Wagner, Joseph J. Luczkovich, and *Richard W. Stoffle*, Multispectral Change Vector Analysis for Monitoring Coastal Marine Environments.

Timothy Rogne, Ian MacDonald, Alexandra Smith, M. C. Kennicutt II, and *Charles Giammona*, Multispectral Remote Sensing and Truth Data from the Tenyo Maru Oil Spill.

Xiuhong Sun and *J. M. Anderson*, A Light-Frequency, Spatially Selecting, Component-Based, Airborne Pushbroom Imaging Spectrometer for Water Environment.

Xiao-Hai Yan and *Laurence C. Breaker*, Surface Circulation Estimation Using Image Processing and Computer Vision Methods Applied to Sequential Satellite Imagery.

A. J. M. Zainal, D. H. Dalby, and *I. S. Robinson*, Monitoring Marine Ecological Changes on the East Coast of Bahrain with Landsat TM.